

# Microstructure and Flame-Resistant Properties of Ti- $X$ V-15Cr ( $X=20, 25, 30, 35$ ) Alloys Prepared by Directed Energy Deposition

Zhang Fengying<sup>1</sup>, Wang Gang<sup>1</sup>, Liu Tong<sup>1</sup>, Wang Kun<sup>1</sup>, Kang Chennuo<sup>1</sup>, Peng Yijie<sup>1</sup>,  
Li Yao<sup>1</sup>, Tan Hua<sup>2</sup>, Chen Yongnan<sup>1</sup>

<sup>1</sup> School of Materials Science and Engineering, Chang'an University, Xi'an 710064, China; <sup>2</sup> State Key Laboratory of Solidification Processing, Northwestern Polytechnical University, Xi'an 710072, China

**Abstract:** A series of Ti- $X$ V-15Cr ( $X=20, 25, 30, 35$ , wt%) alloys were prepared by directed energy deposition (DED) technique, where pure Ti, pure V, and pure Cr powders were used as raw materials. The effects of V content on grain morphology, microhardness, elastic modulus and the flame-resistant properties of Ti- $X$ V-15Cr alloys were investigated. It is found that the microstructures of Ti-20V-15Cr, Ti-25V-15Cr and Ti-30V-15Cr alloys are composed of columnar grains growing epitaxially and fine equiaxed grains at the top region, and the aspect ratio of the columnar grains decreases gradually with increasing the V content. The microstructure of Ti-35V-15Cr alloy is composed of near-equiaxed grains except at the very top region, which is very different from the microstructure of Ti-20V-15Cr, Ti-25V-15Cr and Ti-30V-15Cr alloys. The formation mechanism of microstructure is explained by combining the columnar to equiaxed transition (CET) model and the relationship between the height of the columnar grains layer and  $Z$  axis increment ( $\Delta Z$ ). The average microhardness of Ti- $X$ V-15Cr alloys increases slightly with increasing the V content, and the elastic modulus is between 123.8 and 137.6 GPa. Flame-resistant test shows that Ti-35V-15Cr alloy exhibits the best flame-resistant properties.

**Key words:** Ti-V-Cr alloys; microstructure; directed energy deposition; flame-resistant properties

Titanium and its alloys are vital materials with low density, high specific strength and high heat resistance<sup>[1]</sup>, which are suitable for use in the aerospace, chemical and medical industries. However, once the titanium alloy parts on the engine are burned, they will burn out within 20 s, which means that there is no time to extinguish the fire, eventually leading to serious titanium fire accident, restricting the promotion and application of titanium alloys in advanced aeroengines<sup>[2]</sup>. Considerable efforts have been devoted to designing flame-resistant titanium alloys, which are based on the following methods. (1) Reduce oxygen input in the material. The addition of V and Cr reduces the adiabatic

combustion temperature of titanium, and forms a dense oxide film to inhibit further oxidation of titanium, while the volatilization of  $V_2O_5$  removes excess heat in the combustion area, preventing heat accumulation. (2) Reduce friction. The addition of Cu<sup>[3,4]</sup> forms the  $Ti_2Cu$  phase which has a low melting point, so the titanium alloy parts experience wet friction with liquid lubrication instead of dry friction, which reduces friction heat to the point where it prevents the localized temperature increase<sup>[5]</sup>. The addition of V and Cr for preventing oxygen diffusion is more widely used for this purpose, and a series of alloys have been developed, including alloy C (Ti-35V-15Cr), alloy C<sup>+</sup> (Ti-35V-15Cr-XSi-YC) and

Received date: June 28, 2020

Foundation item: National Key Research and Development Program of China (2016YFB1100103); Natural Science Basic Research Plan in Shaanxi Province of China (2020JM-239); Fundamental Research Funds for the Central Universities CHD (300102319208, 300102310501); National Training Program of Innovation and Entrepreneurship for Undergraduates (S202010710142)

Corresponding author: Zhang Fengying, Ph. D., Professor, School of Materials Science and Engineering, Chang'an University, Xi'an 710064, P. R. China, Tel: 0086-29-82337340, E-mail: zhangfengying@chd.edu.cn

Copyright © 2021, Northwest Institute for Nonferrous Metal Research. Published by Science Press. All rights reserved.

Ti40 (Ti-25V-15Cr-0.2Si). Zhao et al<sup>[6-8]</sup> systematically analyzed the super-high temperature oxidation behavior, deformation and fracture mechanism of Ti40 under hot compression. Zhang et al<sup>[9,10]</sup> reported a special recrystallization mechanism in Ti-35V-15Cr-0.3Si-0.1C alloy and elucidated the influence of TiC on microstructural evolution, describing a relationship between grain size and deformation parameters. Novovic et al<sup>[11]</sup> studied the effect of surface and subsurface condition on the fatigue life of Ti-25V-15Cr-2Al-0.2C alloy, emphasizing on the mechanism of fatigue crack initiation, indicating that the fatigue life depends largely on the carbides and microstructure of the material. Although the Ti-V-Cr series alloys have been widely studied, the preparation of flame-resistant titanium alloy parts using traditional methods faces problems such as low material utilization, high cost (mainly due to the high content of V element) and long processing cycles. Near net shape manufacturing technique provides an effective method to address these problems due to its unique advantages.

Directed energy deposition (DED) is based on the idea of rapid prototyping, which extends the solidification microstructure obtained by laser cladding to 3-D space to achieve high performance and near-net forming of complex parts without using dies<sup>[12]</sup>. In the DED process, the substrate or the previously deposited layer melts by laser beam to form a molten pool, and the raw material powders enter the molten pool via a nozzle, and then the specific geometry is fabricated layer-by-layer. The technical advantages of DED are to provide a novel approach for the design, preparation, and formation of flame-resistant titanium alloys. Wang et al<sup>[13]</sup> used the direct laser fabrication (DLF) to deposit Ti-25V-15Cr-2Al-0.2C on the surface of Ti697 (Ti-11Sn-5Zr-2.25Al-0.25Si), and the small size of the columnar grains and suitable tensile properties were obtained, confirming its

suitability as tip blades. Wu et al<sup>[14,15]</sup> investigated the microstructure, high temperature tensile and creep properties of Ti-25V-15Cr-2Al-0.2C by DLF, and reported that equiaxed grains form in a wide range. In addition, the factors affecting the formation of equiaxed and columnar grains were discussed, and the effect of the oxygen content on the microstructure of the flame-resistant alloy in air was examined. Zhang et al<sup>[16]</sup> detailed the influence of process parameters on the morphology of Ti-25V-15Cr by DED, which confirmed the feasibility of Ti-V-Cr flame-resistant alloys by DED.

In summary, progress of the research about Ti-V-Cr flame-resistant alloys has been made, and the present work focused on the compositions of 25wt%~35wt% V content. However, there are only a few reports on the effect of V on the solidification microstructure and combustion behavior of the flame-resistant titanium alloys by DED. Considering the high cost of V and that adding a large amount of  $\beta$ -stabilizing elements will precipitate a few  $\alpha$  phases on the grain boundaries at high temperature, which is not conducive to the thermal stability of the alloy<sup>[17]</sup>, this work attempts to reduce the V content and analyze its effect on the microstructural evolution and flame-resistant properties of Ti-XV-15Cr ( $X=20, 25, 30, 35$ , wt%) alloys. The mechanical properties were measured using microindentation, providing the basis for performance control and optimization of Ti-V-Cr flame-resistant alloys by DED.

## 1 Experiment

### 1.1 Materials and processing methods

Ti-XV-15Cr ( $X=20, 25, 30, 35$ ) alloys were prepared by melting commercially pure Ti powder, V powder and Cr powder. The purity of the elemental powders exceeds 99.7wt%, and their morphologies and particle sizes are shown in Fig.1. Before the DED process, the powder materials were premixed in a planetary ball mill at a rotation speed of 200

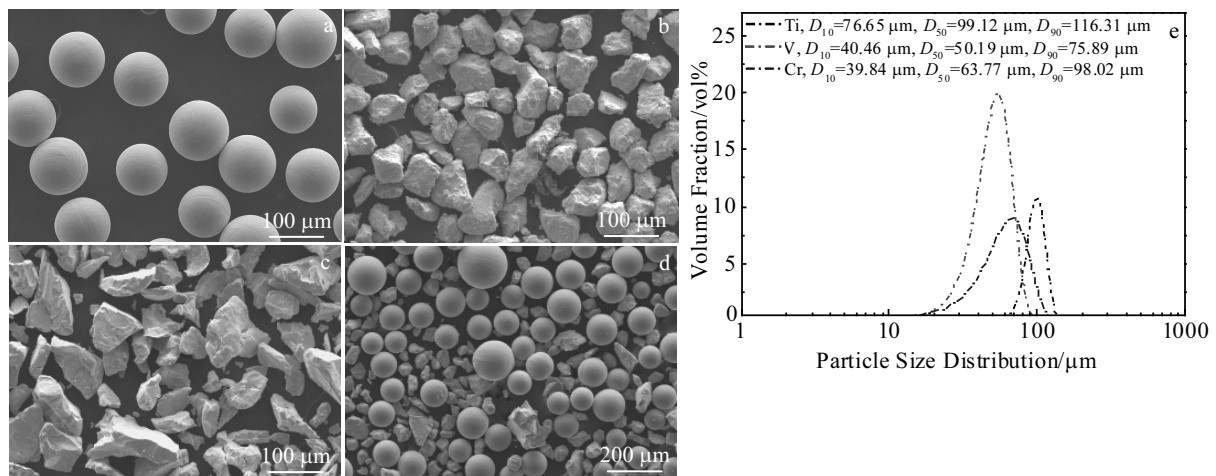


Fig.1 SEM morphologies of Ti (a), V (b), Cr (c) elemental powders and Ti-25V-15Cr blended elemental powders (d); the particle size distribution of different powders (e)

r/min and a ball-to-powder mass ratio of 4:1 for 2 h, and then the mixture was dried under the vacuum condition of  $120\pm 5$  °C to reduce the impact of moisture absorption on the formation quality. The substrate used here was pure Ti plate with a geometric size of 140 mm×50 mm×6 mm, the surface of which was polished using a sandpaper to remove oil and oxide scales, and then it was cleaned by ethanol and acetone before the experiment.

This experiment was conducted through the DED system, consisting of a ~6 kW diode laser with the wavelength of 1.06  $\mu\text{m}$ , a five-axis linkage numerical control working table, an inert atmosphere protection chamber and a coaxial powder feeder nozzle. In order to prevent oxidation and pollution of the alloy during the DED process, the powder carrier gas and protective gas used in the experiment were both high-purity argon, and the oxygen content in the processing chamber was less than 100  $\mu\text{g/g}$ . During the experiment, a reciprocating scanning strategy was used, and the laser beam was incident on the surface of the substrate to form a moving molten pool. The powder particles underwent melting, alloying, and solidification to form a deposited layer which grows along the Z-axis with the scanning direction along the X-axis. The deposition stopped for 5 s after forming each layer to decrease the accumulated heat during the forming process. The used process parameters are presented in Table 1.

### 1.2 Composition and microstructural characterization

The metallographic samples were cut into 10 mm×1.5 mm×10 mm parallel to the scanning direction along the central line (XOZ-plane), and then inlaid, ground, and polished. Kroll reagent (1 vol% hydrofluoric acid and 3 vol% nitric acid in water) was used to etch each sample for 10 s. An OLYMPUS optical microscope (OM) and energy dispersive spectroscopy (EDS) were used to image the as-deposited microstructure and characterize the composition distribution. The selected test points were vertically upward from the bottom to the top along the deposition direction, and the sampling point was chosen every 1 mm. The phase structure was acquired by D8-Advance X-ray diffraction (XRD) with a Cu-K $\alpha$  radiation operated at 40 kV and 40 mA. The grain size involved in this study was measured using Image-Pro Plus. The thermo-physical properties of Ti-XV-15Cr (X=20, 25, 30, 35) alloys were obtained using the Jmat-Pro software, while the length and depth of the molten pool were quantitatively calculated using Mathematica.

### 1.3 Evaluation of microindentation and flame-resistant properties

The microindentation of the deposited samples was conducted using the TUKON 2100 Vickers hardness tester. The indenter used in this work is a standard (diamond)

Berkovich indenter, with a maximum load of 0.196 N and a dwell time of 10 s. The distance between two adjacent test points should be at least three times longer than the diagonal length of the indentation to avoid the influence of deformation near the indentation. From the bottom to the top of the sample, there are sampling points every 2 mm along the deposition direction in this experiment.

The flame-resistant properties of deposited Ti-XV-15Cr alloys were investigated in accordance with GJB 323A-96<sup>[18]</sup>. The test was conducted in the atmosphere with a mixture ratio of oxygen and acetylene at 1.35. The distance between the sample and nozzle was 10 mm, and the ignition time was controlled for 10 s. After combustion, the mass of the samples was measured and calculated to obtain the combustion rate and reflect the flame-resistant properties of the samples.

## 2 Results and Discussion

### 2.1 Composition analysis and phase identification

Fig.2a shows the average chemical compositions of Ti-XV-15Cr (X=20, 25, 30, 35) alloys at different positions from the EDS. The results indicate that the V and Cr contents of the samples are basically consistent with the target compositions, and the fluctuation of element contents is less than 10%.

Fig.2b shows the XRD patterns of Ti-XV-15Cr alloys. It can be seen that the alloys are all mainly composed of body-centered cubic (bcc) single-phase  $\beta$ , and the  $\alpha$  phase is not found. This is due to the high content of  $\beta$ -stabilizing elements V and Cr in Ti-XV-15Cr alloys, resulting in the molybdenum equivalent in the alloys exceeding the critical concentration<sup>[19]</sup>, which completely inhibits the transition from  $\beta$ -Ti to  $\alpha$ -Ti. Therefore, the control and optimization of alloy performance depend more on the morphology of the  $\beta$  grains. The following research focuses on the  $\beta$  grain morphology of Ti-XV-15Cr alloys by DED.

### 2.2 Grain morphology and solidification mechanism

Fig.3 shows the morphologies of  $\beta$  grains of Ti-XV-15Cr (X=20, 25, 30, 35) alloys by DED. It can be seen that the microstructures of the deposited samples are dense with a few defects. The deposited layer of the alloy consists of bright and dark interlaced grains, and a fine equiaxed grain layer can be seen at the top region (Fig.4). With the process parameters shown in Table 1, the bottom and middle deposited layers of Ti-20V-15Cr, Ti-25V-15Cr, Ti-30V-15Cr alloys are composed of irregular columnar grains growing epitaxially. The average width of the columnar grains of Ti-20V-15Cr, Ti-25V-15Cr, and Ti-30V-15Cr alloy is ~476, ~358 and ~319  $\mu\text{m}$ , respectively, while the average length of those alloys is

**Table 1 Process parameters of Ti-XV-15Cr (X=20, 25, 30, 35) alloys prepared by DED**

Laser power/ W	Scanning velocity/ $\text{mm}\cdot\text{min}^{-1}$	Powder feed rate/ $\text{g}\cdot\text{min}^{-1}$	Carrier gas flow/ $\text{L}\cdot\text{h}^{-1}$	$\Delta Z$ / mm	Spot diameter/ mm
2000	600	12	450	0.3	3

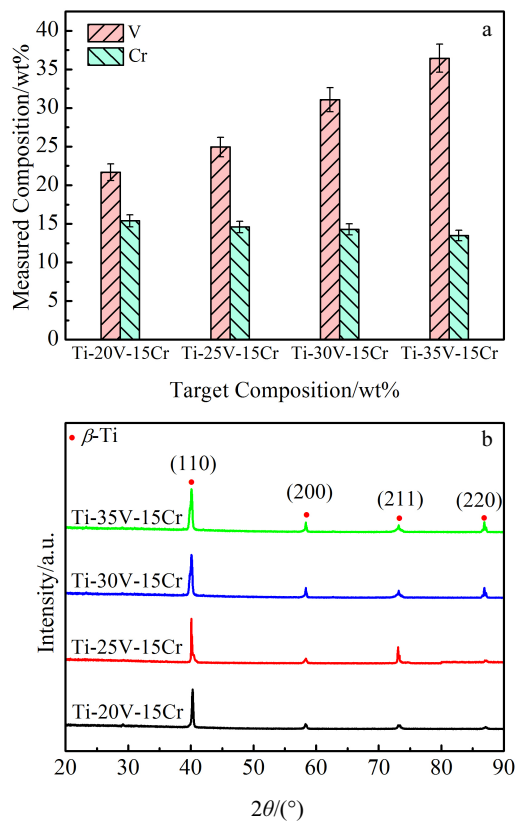


Fig.2 Composition analysis and phase identification of Ti-XV-15Cr ( $X=20, 25, 30, 35$ ) alloys by DED: (a) EDS point scanning results and (b) XRD patterns

~2118, ~1600 and ~1526  $\mu\text{m}$ , respectively. It shows clearly that Ti-25V-15Cr and Ti-30V-15Cr by DED exhibit very similar grains characteristics except Ti-20V-15Cr, but the columnar grains size and aspect ratio significantly reduce. When the V content increases to 35wt%, except the top layer made up of fine equiaxed grains, the middle and lower parts of the deposited sample are almost all near equiaxed grains, which is very different from the microstructure of Ti-20V-15Cr, Ti-25V-15Cr and Ti-30V-15Cr alloys by DED. The average grain width and height of equiaxed grains layer are shown in Fig.5.

Lin et al.<sup>[20,21]</sup> established a columnar to equiaxed transition (CET) model of multicomponent alloys, which is well-used in the prediction of solidification microstructure of titanium alloys by DED<sup>[22]</sup>. Fig.6 presents the CET curves of Ti-XV-15Cr alloys as a function of temperature gradient  $G$  and solidification velocity  $V_s$ , assuming that the solidification velocity  $V_s$  is parallel and equal to the scanning velocity  $V$  at the end of the solidification. It shows that except for Ti-35V-15Cr alloy, the CET curves of Ti-20V-15Cr, Ti-25V-15Cr and Ti-30V-15Cr alloys almost coincide, indicating that the equiaxed layer height of Ti-35V-15Cr is different from that of Ti-XV-15Cr ( $X=20, 25, 30$ ) alloys, which is consistent with the measurement results in

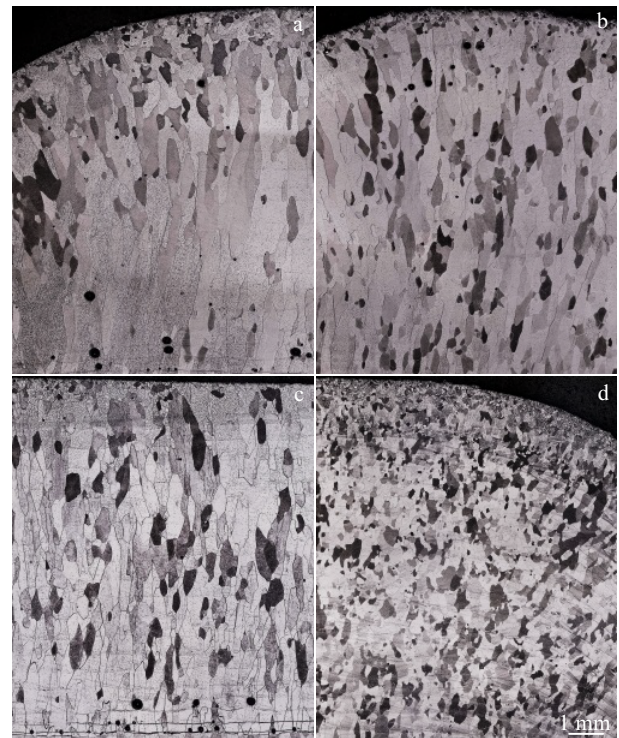


Fig.3 OM images of Ti-20V-15Cr (a), Ti-25V-15Cr (b), Ti-30V-15Cr (c), and Ti-35V-15Cr (d) alloys by DED

Fig.5. However, this does not explain that Ti-35V-15Cr by DED is composed of almost all near equiaxed grains. Actually, DED is a layer-by-layer deposition process. The final grain morphology depends not only on the microstructure formed in a single molten pool, but also on the cumulative results of multiple molten pools, and it is closely related to the remelting of the previous layer during subsequent layer deposition. Although the solidification behavior of those four alloys is similar under the same process parameters, the different thermal physical properties of the alloys may lead to different geometries of the molten pool and further affect the remelting of the subsequent deposited layers, which may be the key factor to influence formation of grains morphology. So the length and depth of the molten pool for Ti-XV-15Cr ( $X=20, 25, 30, 35$ ) by DED are calculated using a 2-D thermal model (Eq.(1)), and the equation is described in Ref.[23].

$$T(x, z, t) = \int_{-D/2}^{D/2} \frac{P\beta}{2\pi\lambda wD} \exp\left[-\frac{v(x-m)}{2\alpha}\right] \int_0^t \frac{dt'}{t'} \exp\left\{-\left[\frac{v^2 t'}{4\alpha} + \frac{(x-m)^2 + z^2}{4\alpha t'}\right]\right\} dm + T_0 \quad (1)$$

where  $x, z$  are the coordinates of the point in the moving coordinate system;  $t$  is time;  $m$  is the  $x$ -coordinate of any line heat source in moving coordinate system ( $m$  varies from  $-D/2$  to  $D/2$ ); other parameters and thermo-physical properties of

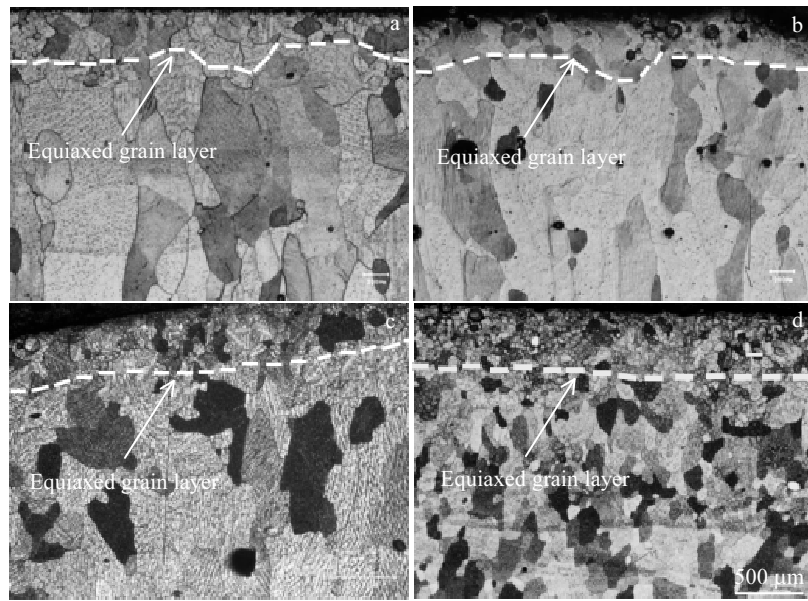


Fig.4 OM images of equiaxed grain layer at the top region of Ti-20V-15Cr (a), Ti-25V-15Cr (b), Ti-30V-15Cr (c), and Ti-35V-15Cr (d) alloys by DED

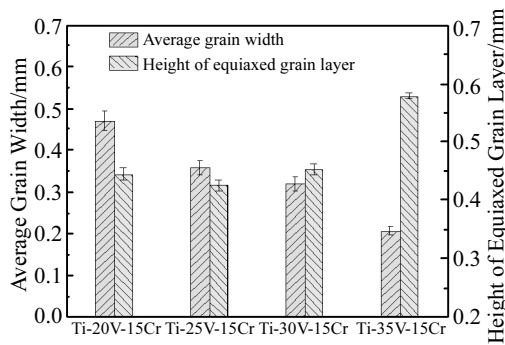


Fig.5 Average grain width and height of equiaxed grain layer of Ti-XV-15Cr (X=20, 25, 30, 35) alloys by DED

Ti-XV-15Cr alloys for the calculation are shown in Table 2. For the convenience of calculation, the laser spot is assumed to be square, and the laser beam side length is equal to the laser spot diameter and the thickness of the thin-wall structure. The thermo-physical properties at 1000 K are selected for calculation, which is based on Ref.[24]. The calculation results of the length and depth of the molten pool are shown in Fig.7.

It can be seen from Fig.7 that the molten pool of Ti-XV-15Cr alloys by DED becomes shorter and shallower with increasing the V content due to the different thermo-physical properties, indicating the lower deposition efficiency with increasing V content. Assuming that the maximum depth of molten pool is equal to the height of deposited layer, the data such as the height of the deposited layer and the height of the equiaxed grain layer are listed in Table 3 through the results

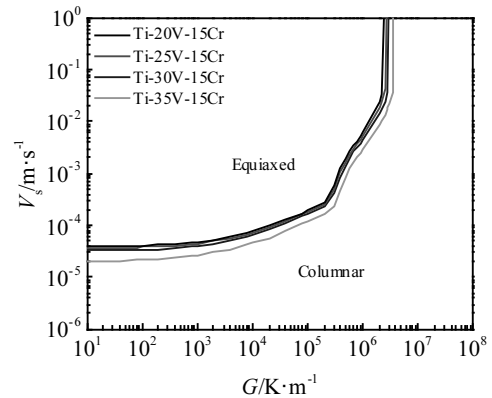


Fig.6 CET curves for Ti-XV-15Cr (X=20, 25, 30, 35) alloys demonstrating the areas of columnar and equiaxed grains as a function of solidification parameters  $G$  (temperature gradient) and  $V_s$  (solidification velocity)

of Fig.5 and 7. In order to explain the formation mechanism of microstructure more clearly, the deposition process is illustrated in Fig.8. It can be seen that the final grain morphology of the deposited samples depends on the relationship between the height of columnar grain layer and  $Z$  axis increment  $\Delta Z$ . When the height of columnar grain layer is greater than  $\Delta Z$ , the equiaxed grains completely remelt to obtain the full columnar grain morphology, such as Ti-20V-15Cr alloy. However, during the deposition process of Ti-30V-15Cr alloy, the equiaxed grain layer of the previous layer remains only about 40  $\mu\text{m}$ , indicating that the equiaxed

**Table 2** Process parameters and thermo-physical properties of Ti-XV-15Cr (X=20, 25, 30, 35) alloys

Parameter	Ti-20V-15Cr	Ti-25V-15Cr	Ti-30V-15Cr	Ti-35V-15Cr
Laser power, $P/W$	2 000	2 000	2 000	2 000
Thermal conductivity, $\lambda/W\cdot\text{mm}^{-1}\cdot\text{K}^{-1}$	0.022 3	0.023 1	0.023 9	0.024 8
Thermal diffusivity, $\alpha/\text{mm}^2\cdot\text{s}^{-1}$	7.27	7.43	7.62	7.77
Laser beam diameter, $D/\text{mm}$	3	3	3	3
Thickness of thin-wall, $w/\text{mm}$	3	3	3	3
Scanning velocity, $v/\text{mm}\cdot\text{s}^{-1}$	10	10	10	10
Absorptivity for diode laser, $\beta$	0.14	0.14	0.14	0.14
Density, $\rho/\text{g}\cdot\text{mm}^{-3}$	0.005 11	0.005 18	0.005 24	0.005 32
Melting point, $T_m/\text{K}$	1 787.7	1 788.1	1 792.0	1 799.4
Substrate temperature, $T_0/\text{K}$	573	573	573	573

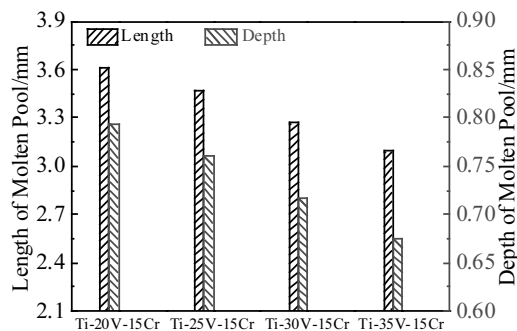


Fig.7 Length and maximum depth of the molten pool for Ti-XV-15Cr (X=20, 25, 30, 35) alloys by DED

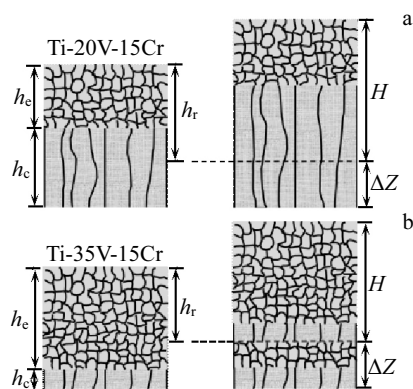
grain layer may not completely melt in some of the deposited layers and interrupt the growth of columnar grains, resulting in the aspect ratio of the columnar grains of Ti-30V-15Cr smaller than that of Ti-20V-15Cr. When the V content increases to 35wt%, the previous equiaxed grain layer can retain 203  $\mu\text{m}$ , and then alternate with the columnar grain layer, so the morphology is almost all near equiaxed.

### 2.3 Discussion on microindentation

Fig.9a shows the load-displacement curves of Ti-XV-15Cr (X=20, 25, 30, 35) alloys under the same loading conditions. The indentation depth of Ti-35V-15Cr is the smallest, while the indentation depth of Ti-20V-15Cr is the largest before reaching the holding stage, indicating that the former has the highest surface hardness. Using the Oliver-Pharr<sup>[25]</sup> model to

**Table 3** Calculated and measured results of Ti-XV-15Cr (X=20, 25, 30, 35) deposited layer (mm)

Parameter	Ti-20V-15Cr	Ti-25V-15Cr	Ti-30V-15Cr	Ti-35V-15Cr
Height of deposited layer, $H$	0.794	0.764	0.717	0.675
Height of equiaxed grain layer, $h_e$	0.445	0.426	0.453	0.578
Height of columnar grain layer, $h_c$	0.349	0.338	0.264	0.097
Z axis increment, $\Delta Z$			0.3	
Remaining height of equiaxed grain layer, $h_{re}$	0	0	0.036	0.203



$h_e$  — Height of equiaxed area  $H$  — Height of deposited layer  
 $h_c$  — Height of columnar area  $h_r$  — Depth of remelting area  
 $\Delta Z$  — Z axis increment

Fig.8 Schematic diagram of the microstructure formation of Ti-20V-15Cr (a) and Ti-35V-15Cr (b) alloys by DED

analyze the unloading part of the load-displacement curves, the average hardness and elastic modulus are obtained and shown in Fig.9d. It can be seen that with increasing V content, the hardness of Ti-XV-15Cr increases from 4.18 GPa to 4.77 GPa due to the lattice distortion caused by the dissolution of V. The elastic modulus is between 123.8 and 137.6 GPa.

The load-displacement curves can be used to determine the initial plastic deformation behavior of materials. The first “pop-in”<sup>[26]</sup> events in the loading stage are related to the elastic-plastic transformation of materials. It is generally believed that the reason for the “pop-in” phenomenon of the load-displacement curve is that the shear stress of the material reaches a critical value under the action of the indenter, and a lot of nucleation and proliferation of dislocations lead to microstructural changes. As shown in Fig.9a, the four loading curves are smooth without the pop-in phenomenon, indicating that the deformation at this stage is purely elastic, and there is no crack or brittle fracture in the materials during the loading process.

Observing the enlarged drawing (Fig.9a) of the holding stage, it can be found that the creep depth of the samples with various V contents is different, and the creep depth of Ti-20V-15Cr sample is the largest, while that of Ti-35V-15Cr is the smallest, and between them the creep depth of Ti-25V-15Cr and Ti-30V-15Cr falls with little difference. Simultaneously, there are fluctuations in the creep depth-time curves (Fig.9b), which may be due to the large temperature difference between the sample and indenter. The creep rate-time relationship curves of Ti-XV-15Cr alloys shown in Fig.9c can be used to better analyze the creep behavior of the samples. The results show that the creep process of the materials can be divided into two stages: rapid creep and stable creep. It is generally believed that the period of rapid creep at the beginning is relatively short, mainly dominated by strain hardening, and then it reaches to the dominant stage of viscous deformation caused by dislocation migration, which is the stable creep stage of materials, where there are no significant differences in the creep rate of Ti-XV-15Cr alloys, confirming that the creep mechanism of Ti-XV-15Cr alloys with different V contents is similar at room temperature.

#### 2.4 Analysis of flame-resistant mechanism

The combustion rate of Ti-XV-15Cr ( $X=20, 25, 30, 35$ ) alloys is calculated to reflect the flame-resistant properties. The combustion rate is defined as follows:

$$v = \frac{m_1 - m_0}{t} \quad (2)$$

where  $v$  is the combustion rate of the sample ( $\text{mg}\cdot\text{s}^{-1}$ );  $m_1$  is the mass of sample after combustion (mg);  $m_0$  is the mass of sample before combustion (mg);  $t$  is the combustion time (s).

The combustion rate of Ti-XV-15Cr alloys can be calculated by Eq.(2), and the results are shown in Table 4. In combustion, oxygen enters the substrate and reacts with elements, so the greater mass gain indicates a more violent reaction and a higher combustion rate. It can be seen from Table 4 that the flame-resistant properties of Ti-XV-15Cr alloy by DED are gradually enhanced with increasing the V content. Although the combustion rate of Ti-20V-15Cr is the highest among the four alloys, its combustion rate is still a little lower than that of forged Ti40 under the same experimental conditions (the combustion rate of forging Ti40 is  $8.2 \text{ mg}\cdot\text{s}^{-1}$ ) due to the formation of subgrains in the local region of Ti-25V-15Cr alloy, which makes V and Cr easily diffuse to the surface under heating conditions, thereby inhibiting the reaction of Ti and O<sup>[27]</sup>. The more in-depth mechanism still needs further study.

The combustion process of titanium alloy is similar to the oxidation process, which is the reaction of matrix metal or alloying elements with oxygen. It can be seen from the oxygen potential diagram<sup>[28]</sup> (Fig.10) of Ti-O, V-O and Cr-O that the Gibbs free energy of Ti reacting with O<sub>2</sub> to produce TiO<sub>2</sub> is the smallest, followed by V, and Gibbs free energy of Cr is the highest. Therefore, Ti takes precedence over V and Cr to form oxides, and the oxidation of Ti is the main process of combustion. The electronegativity of Ti is lower than that of V and

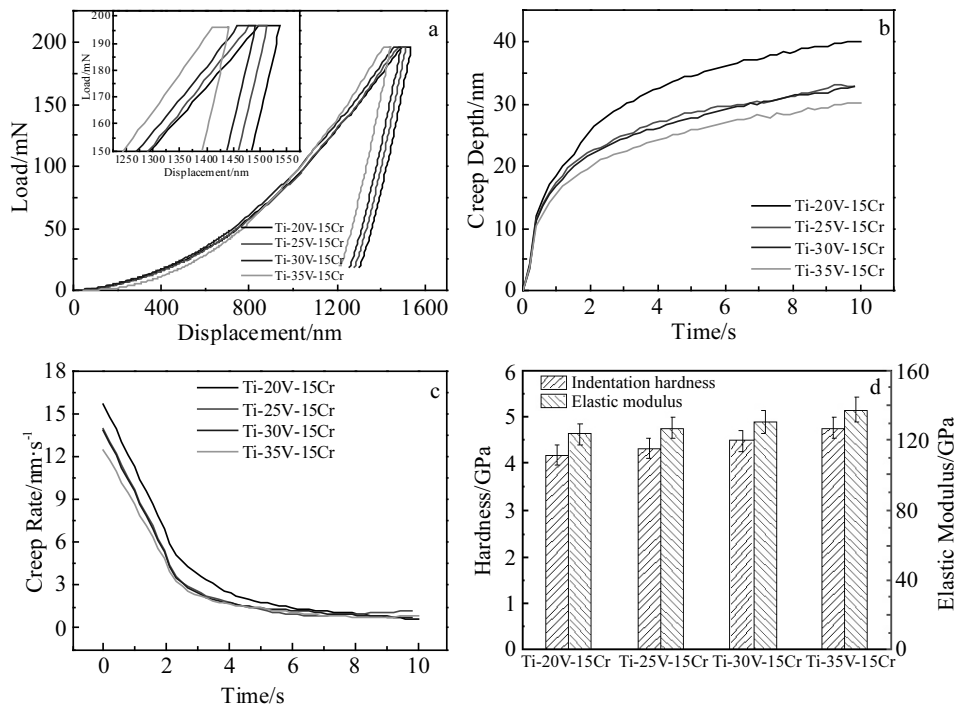
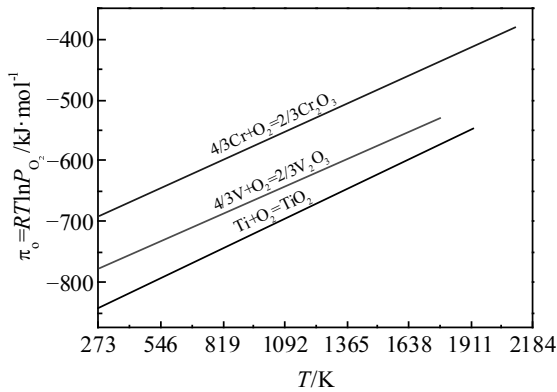


Fig.9 Microindentation results of Ti-XV-15Cr ( $X=20, 25, 30, 35$ ) alloys by DED: (a) load-displacement curves, (b) creep depth-holding time curves, (c) relationship between creep rate and holding time, and (d) average hardness and elastic modulus

**Table 4** Combustion rate of Ti-XV-15Cr (X=20, 25, 30, 35) alloys by DED

Samples	Ti-20V-15Cr	Ti-25V-15Cr	Ti-30V-15Cr	Ti-35V-15Cr
Combustion rate/mg·s <sup>-1</sup>	7.3	7.0	6.1	5.8

Fig.10 Oxygen potential diagram of Ti-O, V-O and Cr-O<sup>[28]</sup>

Cr (the electronegativity of Ti, V and Cr is 1.54, 1.63 and 1.66, respectively), and the affinity of these elements with O decreases in turn, which further indicates that Ti is the most likely to react with O.

The diffusion activation energy of Ti, V and Cr in titanium alloy is 293.2, 134.8, and 167 kJ·mol<sup>-1</sup>, respectively<sup>[29]</sup>. Therefore, the probability of V and Cr atoms being activated and migrated is greater than that of Ti. According to the oxygen potential diagram, the surface combustion product is mainly dense oxides of Ti and V, which prevent the diffusion of oxygen into the matrix. At the same time, the enrichment of V and Cr elements in the inner surface layer hinders the diffusion of Ti to the combustion product area. In conclusion, the formation of dense oxides in the combustion area and the enrichment of V and Cr slow down the further reaction between Ti and O, which improves the flame-resistant properties of Ti-XV-15Cr alloys with increasing the V content.

### 3 Conclusions

1) The microstructures of Ti-XV-15Cr (X=20, 25, 30) alloys are composed of columnar grains growing epitaxially and fine equiaxed grains at the top region, while Ti-35V-15Cr alloy is composed of near-equiaxed grains except at the very top region. This can be explained by the columnar to equiaxed transition (CET) model and the relationship between the height of the columnar grains layer and Z axis increment ( $\Delta Z$ ).

2) With increasing the V content, the microhardness, elastic modulus and creep resistance of Ti-XV-15Cr alloys increase gradually mainly due to the lattice distortion caused by the solution of V. There is no “pop-in” phenomenon on the load-displacement curves, indicating that no cracks or brittle fractures occur during loading.

3) When the content of V is between 20wt%~35wt%, the

flame-resistant properties of Ti-XV-15Cr alloys by DED improve gradually due to the low diffusion activation energy and high Gibbs free energy of V and Cr, and the flame-resistant properties of Ti-20V-15Cr are better than those of forged Ti40.

### References

- Zhao Y Q, Zhou L, Deng J. *Journal of Alloys and Compounds*[J], 1999, 284(1-2): 190
- Mi G B, Huang X S, Li P J et al. *Transactions of Nonferrous Metals Society of China*[J], 2012, 22(10): 2409
- Chen Y N, Yang W Q, Bo A et al. *Materials and Design*[J], 2018, 156: 588
- Yan L L, Yu Z, Jie J Y et al. *Surface and Coatings Technology*[J], 2020, 392: 125 697
- Shao L, Wang Y Y, Xie G L et al. *Materials*[J], 2019, 12(19): 3206
- Zhao Y Q, Xin S W, Zeng W D. *Journal of Alloys and Compounds*[J], 2009, 481(1-2): 190
- Han Y F, Zeng W D, Zhao Y Q et al. *Materials & Design*[J], 2010, 31(9): 4380
- Zhu Y C, Zeng W D, Zhang F S et al. *Materials Science and Engineering A*[J], 2012, 553: 112
- Zhang S F, Zeng W D, Gao X X et al. *Journal of Alloys and Compounds*[J], 2016, 684: 201
- Zhang S F, Zeng W D, Zhou D D et al. *Materials Letters*[J], 2016, 166: 317
- Novovic D, Aspinwall D K, Dewes R C et al. *CIRP Annals*[J], 2016, 65(1): 523
- Huang W D. *Laser Solid Forming*[M]. Xi'an: Northwestern Polytechnical University Press, 2007: 340 (in Chinese)
- Wang F D. *Metallurgical and Materials Transactions A*[J], 2012, 43(2): 677
- Wu X H, Sharman R, Mei J F et al. *Materials and Design*[J], 2002, 23(3): 239
- Wu X H, Sharman R, Mei J F et al. *Materials and Design*[J], 2004, 25(2): 103
- Zhang F Y, Liu T, Zhao H Y et al. *International Journal of Advanced Manufacturing Technology*[J], 2017, 91: 1461
- Zhao Y Q, Qu H L, Wang M M et al. *Journal of Alloys and Compounds*[J], 2006, 407(1-2): 118
- Hu M X, Wang J, Li A F et al. *Test Methods for Ablation of Ablators: GJB 323A-96*[S]. Beijing: National Defense Military Standard Press, 1996 (in Chinese).
- Froes F H, Bomberger H B. *JOM*[J], 1985, 37(7): 28
- Lin X, Li Y M, Wang M et al. *Science in China Series E-Technological Sciences*[J], 2003, 46(5): 475
- Lin X, Yue T M, Yang H O et al. *Materials Science and Engineering A*[J], 2005, 391(1-2): 325

- 22 Zhang F Y, Yang M, Clare A T et al. *Journal of Alloys and Compounds*[J], 2017, 727: 824
- 23 Tan H, Chen J, Zhang F Y et al. *International Journal of Machine Tools and Manufacture*[J], 2010, 50(1): 2
- 24 Tan H, Chen J, Zhang F Y et al. *Optics & Laser Technology*[J], 2010, 42(1): 50
- 25 Oliver W C, Pharr G M. *Journal of Materials Research*[J], 1992, 7(6): 1566
- 26 Navamathavan R, Moon Y T, Kim G S et al. *Materials Chemistry and Physics*[J], 2006, 99(2-3): 410
- 27 Zhang F Y, Mei M, Yang X K et al. *Rare Metal Materials and Engineering*[J], 2018, 47(6): 1771 (in Chinese)
- 28 Huang X H. *Principles of Iron and Steel Metallurgy*[M]. Beijing: Metallurgical Industry Press, 2013: 352 (in Chinese)
- 29 Gerhard N, Cornelis T. *Self-Diffusion and Impurity Diffusion in Pure Metals*[M]. Oxford: Pergamon, 2008: 151

## 直接能量沉积 Ti-XV-15Cr (X=20, 25, 30, 35)合金的组织 and 阻燃性能

张凤英<sup>1</sup>, 王刚<sup>1</sup>, 刘桐<sup>1</sup>, 王坤<sup>1</sup>, 康晨诺<sup>1</sup>, 彭艺杰<sup>1</sup>, 李尧<sup>1</sup>, 谭华<sup>2</sup>, 陈永楠<sup>1</sup>

(1. 长安大学 材料科学与工程学院, 陕西 西安 710064)

(2. 西北工业大学 凝固技术国家重点实验室, 陕西 西安 710072)

**摘要:** 使用直接能量沉积技术, 以纯 Ti、纯 V 和纯 Cr 粉末为原料制备一系列 Ti-XV-15Cr (X=20, 25, 30, 35)合金。研究了 V 含量对 Ti-XV-15Cr 合金的晶粒形貌、显微硬度、弹性模量及阻燃性能的影响。结果表明, Ti-20V-15Cr、Ti-25V-15Cr 和 Ti-30V-15Cr 合金的显微组织由外延生长的柱状晶和顶部细小的等轴晶组成, 随着 V 含量的增加, 柱状晶粒的长/宽比逐渐减小。而 Ti-35V-15Cr 合金的显微组织与 Ti-20V-15Cr、Ti-25V-15Cr 和 Ti-30V-15Cr 有很大的不同, 除了顶部是细小的等轴晶, 几乎全由近等轴晶组成。结合柱状晶向等轴晶转变 (CET) 模型以及柱状晶层的高度与 Z 轴抬升量 ( $\Delta Z$ ) 之间的关系, 解释了微观组织的形成机理。Ti-XV-15Cr 合金的平均显微硬度随 V 含量的增加而略有增加, 其弹性模量在 123.8 与 137.6 GPa 之间。阻燃测试表明, Ti-35V-15Cr 合金具有最佳的阻燃性能。

**关键词:** Ti-V-Cr 合金; 显微组织; 直接能量沉积; 阻燃性能

---

作者简介: 张凤英, 女, 1980 年生, 博士, 教授, 长安大学材料科学与工程学院, 陕西 西安 710064, 电话: 029-82337340, E-mail: zhangfengying@chd.edu.cn